

Multiband Nature of the Room-Temperature Superconductivity in Compressed LaH₁₀

Chongze Wang, Seho Yi, and Jun-Hyung Cho*

*Department of Physics, Research Institute for Natural Science,
and HYU-HPSTAR-CIS High Pressure Research Center, Hanyang University,
222 Wangsimni-ro, Seongdong-Ku, Seoul 04763, Republic of Korea*

(Dated: October 15, 2019)

Recently, the discovery of room-temperature superconductivity (SC) was experimentally realized in the fcc phase of LaH₁₀ under megabar pressures. This SC of compressed LaH₁₀ has been explained in terms of strong electron-phonon coupling (EPC), but the mechanism of how the large EPC constant and high superconducting transition temperature T_c are attained has not yet been clearly identified. Based on the density-functional theory and the Migdal-Eliashberg formalism, we reveal the presence of two nodeless, anisotropic superconducting gaps on the Fermi surface (FS). Here, the small gap is mostly associated with the hybridized states of H s and La f orbitals on the three outer FS sheets, while the large gap arises mainly from the hybridized state of neighboring H s or p orbitals on the one inner FS sheet. Further, we find that the EPC constant of compressed YH₁₀ with the same sodalite-like clathrate structure is enhanced due to the two additional FS sheets, leading to a higher T_c than LaH₁₀. It is thus demonstrated that the multiband pairing of hybridized electronic states is responsible for the large EPC constant and room-temperature SC in compressed hydrides LaH₁₀ and YH₁₀.

PACS numbers:

The realization of superconductivity (SC) at room temperature is one of the most challenging subjects in modern physics and chemistry. Recently, two experimental groups synthesized the lanthanum hydride LaH₁₀ with a sodalite-like clathrate structure [see Fig. 1(a)] at megabar pressures and measured a superconducting transition temperature T_c of 250–260 K at a pressure of ~ 170 GPa [1, 2]. Obviously, this record of T_c is the highest among so far experimentally available superconducting materials [3–6], thereby opening a new era of high- T_c SC [7, 8].

Historically, a search for room-temperature SC in compressed hydrides dates back to about half a century ago. Based on the Bardeen-Cooper-Schrieffer (BCS) theory [9], Neil Ashcroft [10] proposed a pioneering idea that the metallization of hydrogen under high pressures over ~ 400 GPa could exhibit a high- T_c SC [11–13]. Since then, in order to achieve metallic hydrogen at relatively lower pressures attainable using diamond anvil cells [14, 15], many binary hydrides have been theoretically searched [7, 8, 16–22], among which rare-earth hydrides such as the fcc phases of YH₁₀ and LaH₁₀ exhibited room-temperature SC at around 200–300 GPa [21, 22]. Recently, a number of density functional theory (DFT) studies [21–26] have been intensively performed to show that fcc LaH₁₀ having a high crystalline symmetry of the space group $Fm\bar{3}m$ (No. 225) with the point group O_h features the peculiar bonding characters with anionic La, anionic H₁ [forming the squares in Fig. 1(a)], and cationic H₂ [forming the hexagons in Fig. 1(a)] atoms, van Hove singularities near the Fermi energy E_F , and strong electron-phonon coupling (EPC) with H-derived phonon modes. These unique bonding, electronic, and phononic properties of fcc LaH₁₀ have been associated with increased EPC constant, leading to the emergence of a room-temperature SC. However, the detailed underlying mechanism of how fcc LaH₁₀ forms the large EPC constant and high T_c remains to be clarified.

In this Letter, using the DFT calculations [27] and the

Migdal-Eliashberg formalism [28–30], we explore the nature of superconducting gap in fcc LaH₁₀. Our analysis of the momentum-resolved superconducting gap reveals that there are two nodeless, anisotropic superconducting gaps on the Fermi surface (FS), representing a two-gap SC with s -wave symmetry. It is found that at 20 K, the small gap in the range of 41–52 meV is mostly associated with the hybridized states of H₁ s and La f orbitals on the three outer FS sheets, while the large gap in the range of 60–66 meV arises mainly from the hybridized state of H₁ s or p and H₂ s orbitals on the one inner FS sheet. Interestingly, for fcc YH₁₀ having the same sodalite-like clathrate structure, we find that the four FS sheets whose patterns are similar to those of fcc LaH₁₀ slightly shift upward because the two additional FS sheets arising from Y d orbitals are occupied. The resulting six FS sheets of fcc YH₁₀ not only contribute to increase the EPC constant due to the increased electron-phonon scattering channels but also produce the two gaps widely distributed in the range of 41–75 meV at 20 K, leading to a higher T_c than fcc LaH₁₀. Therefore, we demonstrate that the underlying mechanism of the large EPC constant and room-temperature SC in compressed hydrides LaH₁₀ and YH₁₀ can be traced to the multiband pairing of hybridized electronic states.

We first present the electronic band structure of fcc LaH₁₀, obtained using the DFT calculations [31]. In all the calculations hereafter, we fix a pressure of 300 GPa favoring the fcc phase of LaH₁₀ [21–23, 26], where the optimized lattice parameters are $a = b = c = 4.748$ Å. As shown in Fig. 1(b), the calculated band structure exhibits four bands (denoted as $n = 1, 2, 3,$ and 4) crossing E_F . The corresponding FS sheets are displayed in Fig. 1(c), together with the projection of their electronic states onto the constituent atoms H₁, H₂, and La. The first FS sheet with the polyhedron shape around the X point is mostly composed of a hybridized state of H₁ s and La f orbitals (see Fig. S1 in the Supplemental Material [41]). The second FS sheet with the complex shape

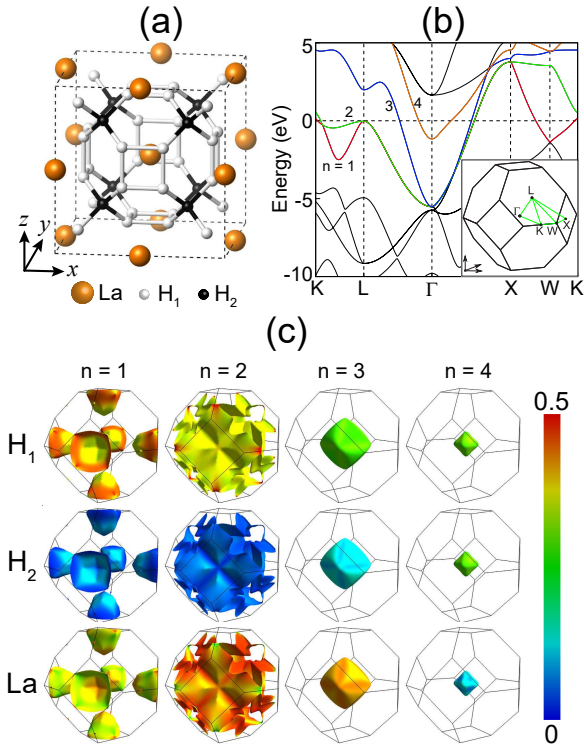


FIG. 1: (Color online) (a) Optimized structure of the fcc phase of compressed LaH_{10} , composed of the cages of 32 H atoms surrounding a La atom. The two different types of H atoms, i.e., H_1 and H_2 , are drawn with bright and dark circles, respectively. The positive x , y , and z axes point along the $[001]$, $[010]$, and $[001]$ directions, respectively. (b) Calculated band structure of fcc LaH_{10} and (c) the corresponding FS sheets for the four bands of $n = 1, 2, 3$, and 4. The inset of (b) shows the Brillouin zone of the fcc primitive cell, where the Γ -X line is parallel to the x axis. In (c), the electronic state at each FS sheet is projected onto H_1 , H_2 , and La atoms using the color scale in the range $[0, 0.5]$.

spreading over the large outer regions of Brillouin zone is also composed of a hybridized state of H_1 s and La f orbitals (see Fig. S1 in the Supplemental Material [41]). The third and fourth FS sheets are topologically quite similar with concentric polyhedron shapes around the Γ point. However, these FS sheets have different orbital characters: i.e., the third one arises largely from a hybridized state of H_1 s and La f orbitals, whereas the fourth one is mainly due to a hybridized state of H_1 s or p and H_2 s orbitals (see Fig. S1 in the Supplemental Material [41]). It is noticeable that such hybridized electronic states near E_F could effectively screen the lattice vibrations involving H atoms, thereby giving rise to a strong EPC in fcc LaH_{10} . Further, the FS sheets with different orbital characters are expected to invoke different couplings between the various bands, leading to the emergence of anisotropic multiple SC gaps, as will be demonstrated later.

To illustrate an overview of the EPC and T_c of fcc LaH_{10} , we calculate the Eliashberg function $\alpha^2F(\omega)$ and integrated EPC constant $\lambda(\omega)$ using the isotropic Migdal-Eliashberg equations [28–30]. The calculated results together with the

logarithmically average phonon frequency ω_{log} are displayed in Fig. 2(a). We find that $\lambda(\omega)$ increases monotonously as ω increases up to the optical phonon modes with a high frequency of $\sim 1800 \text{ cm}^{-1}$, indicating that the lattice vibrational modes in the whole frequency range participate in the increase of $\lambda(\omega)$. It is noted that the four FS sheets distributed over the whole Brillouin zone provide the EPC channels with many phonon modes of widely distributed \mathbf{q} wavevectors. Using the McMillan-Allen-Dynes formula [42], we estimate T_c as a function of ω [see Fig. 2(a)]. Although the McMillan-Allen-Dynes formula cannot properly describe anisotropic multi-band SC, its estimation of $T_c(\omega)$ may give a qualitative aspect of how largely certain-frequency phonon modes contribute to T_c . As shown in Fig. 2(a), H-derived optical phonon modes contribute to a nearly linear increase of T_c with increasing ω . It is, however, interesting to note that, even though the acoustic phonon modes of La atoms provide $\sim 12\%$ of the total EPC constant $\lambda = \lambda(\infty)$ [23, 26], they hardly contribute to an increase of T_c [see Fig. 2(a)].

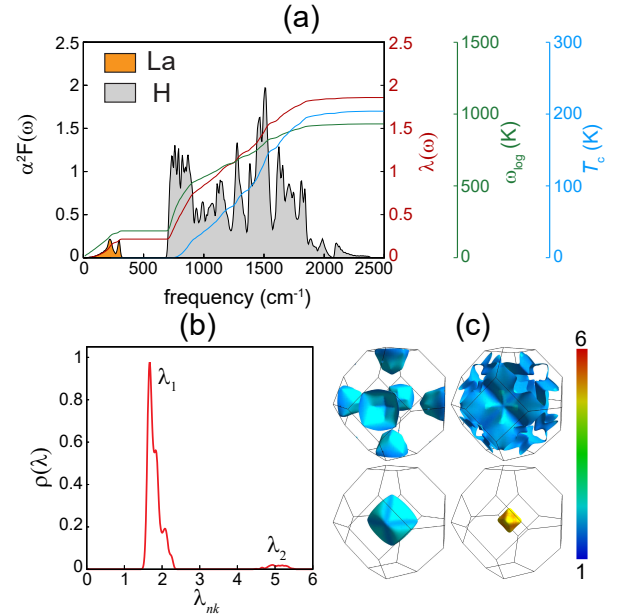


FIG. 2: (Color online) (a) Isotropic Eliashberg function $\alpha^2F(\omega)$ (black), integrated EPC constant $\lambda(\omega)$ (red), ω_{log} (green), and T_c (blue) of fcc LaH_{10} . (b) Distribution of \mathbf{k} -resolved EPC constant $\lambda_{n\mathbf{k}}$ and (c) the projected $\lambda_{n\mathbf{k}}$ on each FS sheet. In (b), the two separated regimes of $\lambda_{n\mathbf{k}}$ are indicated as λ_1 and λ_2 .

In order to examine the anisotropy in the EPC of fcc LaH_{10} , we use the anisotropic Migdal-Eliashberg equations [28–30] to calculate the \mathbf{k} -resolved EPC constant $\lambda_{n\mathbf{k}}$ for the electronic state (n, \mathbf{k}) , which includes all available electron-phonon scattering processes connecting \mathbf{k} and other \mathbf{k} points on the FS sheets. The distribution of $\lambda_{n\mathbf{k}}$ and their projection on each FS sheet are plotted in Figs. 2(b) and 2(c), respectively. We find that there are two regimes of $\lambda_{n\mathbf{k}}$: i.e., the lower regime λ_1 in the range of 1.55–2.29 arising from the $n = (1, 2, 3)$ bands and the upper one λ_2 in the range of 4.49–5.49 arising

from the $n = 4$ band. Here, it is noticeable that (i) the larger distribution of λ_1 is caused by the high density of states (DOS) of the hybridized $n = (1, 2, 3)$ states at E_F , and (ii) the larger λ_2 values represent the strong EPC of the hybridized $n = 4$ state stemming from H_1 s or p and H_2 s orbitals. Thus, the division of the two regimes λ_1 and λ_2 indicates the different EPC strengths depending on the orbital characters of the hybridized electronic states on the FS sheets. We also note that some spreads of the λ_1 and λ_2 values feature the anisotropy of EPC, which is apparent from the projection of λ_{nk} on each FS sheet: i.e., the size of λ_{nk} changes with respect to the \mathbf{k} directions on each FS sheet [see Fig. 2(c)].

It is natural that the two well-separated regimes of λ_{nk} in fcc LaH_{10} could give rise to two superconducting gaps. By numerically solving the anisotropic Migdal-Eliashberg equations [28–30] with a typical Coulomb pseudopotential parameter of $\mu^* = 0.13$ [21, 22], we calculate the temperature dependence of superconducting gap Δ . Figure 3(a) displays the energy distribution of Δ as a function of temperature. We find that there are the two gaps Δ_1 and Δ_2 , indicating a two-gap SC. These two gaps close at $T_c \approx 252$ K [see Fig. S2(a) in the Supplemental Material [41]]. For $T < 100$ K, Δ_1 is distributed in the range of 41–52 meV, while Δ_2 in the range of 60–66 meV. From the \mathbf{k} -resolved superconducting gap Δ_{nk} on the four FS sheets [see Fig. 3(b)], we find that the formation of Δ_1 is associated with the FS sheets of $n = 1, 2,$ and 3 , while that of Δ_2 arises from the FS sheet of $n = 4$. Thus, we can say that λ_{nk} and Δ_{nk} are correlated with each other: i.e., the larger the magnitude of λ_{nk} , the higher is the Δ_{nk} value. It is noticeable that the size of Δ_{nk} changes on each FS sheet without any node, representing the anisotropic superconducting gaps with s -wave symmetry. In Fig. 3(a), the Δ values obtained from the isotropic Migdal-Eliashberg formalism are also plotted with the dashed line. Here, the gap closes around $T_c \approx 233$ K, smaller than that ($T_c \approx 252$ K) estimated from the anisotropic Migdal-Eliashberg formalism, but both values are much larger than that (~ 204 K) obtained using the McMillan-Allen-Dynes formula [42].

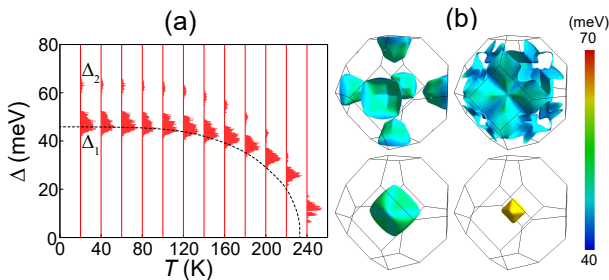


FIG. 3: (Color online) (a) Energy distribution of the anisotropic superconducting gap Δ of fcc LaH_{10} . The two separated gaps are indicated as Δ_1 and Δ_2 . The dashed line in (a) represents the Δ values, estimated using the isotropic Migdal-Eliashberg equations. (b) \mathbf{k} -resolved superconducting gap Δ_{nk} on the four FS sheets, computed at 20 K.

Based on our results of λ_{nk} and Δ_{nk} in fcc LaH_{10} , we con-

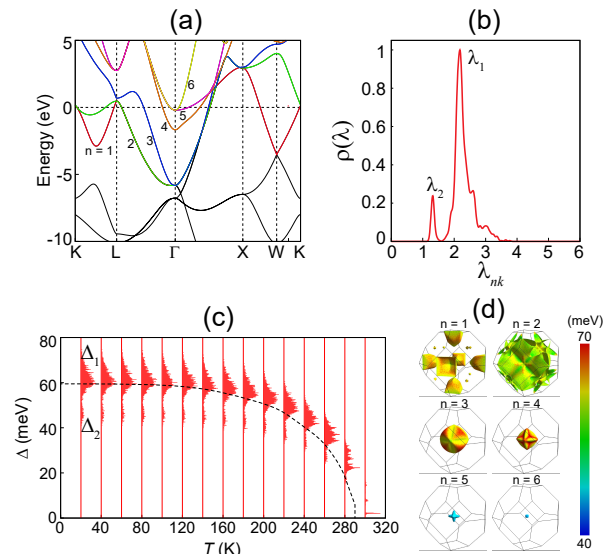


FIG. 4: (Color online) (a) Calculated band structure of fcc YH_{10} at 300 GPa and (b) the distribution of λ_{nk} . In (b), the two regimes of λ_{nk} are indicated as λ_1 and λ_2 . (c) Energy distribution of Δ as a function of temperature and (d) Δ_{nk} on the six FS sheets, computed at 20 K. The dashed line in (c) represents Δ estimated using the isotropic Migdal-Eliashberg equations.

clude that the predicted anisotropic EPC and superconducting gaps are attributed to the multiband pairing with the four FS sheets composed of the hybridized states of different orbital characters [see Fig. 1(c)]. To further demonstrate the importance of multiband pairing in high- T_c SC, we study the properties of λ_{nk} and Δ_{nk} of fcc YH_{10} that was previously [20–22] predicted to exhibit higher T_c than fcc LaH_{10} . The geometry of fcc YH_{10} is the same sodalite-like clathrate structure as fcc LaH_{10} (see Fig. S3 in the Supplemental Material [41]). Figure 4(a) shows the calculated electronic band structure of fcc YH_{10} at 300 GPa. We find that fcc YH_{10} has very similar dispersions for the four bands of $n = 1, 2, 3,$ and 4 , as compared with those of fcc LaH_{10} [see Fig. 1(b)]. However, in fcc YH_{10} , the two electron-like bands of $n = 5$ and 6 originating mostly from Y d orbitals become occupied below E_F around the Γ point [see Fig. 4(a) and Fig. S4 in the Supplemental Material [41]]. Therefore, fcc YH_{10} has the six FS sheets which provide more EPC channels, leading to the enhancements of the EPC constant and T_c . Using the isotropic Migdal-Eliashberg formalism [28–30], we obtain $\lambda = 2.23$ and $T_c = 290$ K, larger than those ($\lambda = 1.86$ and $T_c = 233$ K) of fcc LaH_{10} . Figure 4(b) shows the calculated distribution of anisotropic λ_{nk} in fcc YH_{10} , where the peaks of the two regimes λ_1 and λ_2 locate at around 2.19 and 1.33, respectively. From the projection of λ_{nk} on each FS sheet, we find that λ_1 originates mostly from the $n = (1, 2, 3, 4)$ bands, while λ_2 is due to the $n = (5, 6)$ bands [see Fig. S5 in the Supplemental Material [41]]. Compared with the large λ_{nk} values (between 4.49–5.49) originating from the $n = 4$ band of fcc LaH_{10} [see Figs. 2(b) and 2(c)], the corresponding values of

fcc YH₁₀ are much reduced to about 2.20–3.79 (see Fig. S5), which reflects the weakened intraband and interband coupling strengths of the $n = 4$ band as the $n = 5$ and 6 bands are occupied. However, the λ_{nk} values of the $n = (1, 2, 3)$ bands in fcc YH₁₀ increase by ~ 0.5 , compared to the corresponding values in fcc LaH₁₀ [see the peak positions of λ_1 in Figs. 2(b) and 4(b), as well as the the projected λ_{nk} on each FS sheet in Figs. 2(c) and S5]. It is noted that the $n = (5, 6)$ bands having weak hybridization characters (see Fig. S4 in the Supplemental Material [41]) give rise to relatively smaller values of λ_2 [see Fig. 4(b)]. Figures 4(c) and 4(d) show the temperature dependence of Δ and the \mathbf{k} -resolved Δ_{nk} on the six FS sheets, respectively. These results agree well with those obtained by a recent first-principles calculation of Heil *et al.* [20]. As shown in Fig. 4(c), for $T < 100$ K, Δ consisting of the two gaps Δ_1 and Δ_2 is widely distributed between 41 and 75 meV. This broad gap closes at $T_c \approx 308$ K [see Fig. S2(b) in the Supplemental Material [41]], higher than that [~ 252 K in Fig. 3(a)] of fcc LaH₁₀. We note that the large gap Δ_1 arises from the $n = (1, 2, 3, 4)$ bands, while the small gap Δ_2 is due to the $n = (5, 6)$ bands [see Fig. 4(d)]. It is thus demonstrated that the multiband pairing of fcc YH₁₀ with the six FS sheets gives rise to higher T_c than fcc LaH₁₀ with the four FS sheets.

Since the minima of the $n = (5, 6)$ bands of fcc YH₁₀ are close to E_F , they are enabled to be unoccupied by the hole doping of $n_h > \sim 0.17e$ per unit cell (see Fig. S6 in the Supplemental Material [41]). In order to examine how the occupation of the $n = (5, 6)$ bands influences SC, we use the isotropic Migdal-Eliashberg formalism [28–30] to estimate the variations of λ and T_c with respect to the amount of n_h . We find that λ and T_c decrease monotonously with increasing n_h (see Table SI in the Supplemental Material [41]). As a result, T_c decreases from 290 K (without hole doping) to 269 K at $n_h = 0.3e$. It is thus manifested that the reduced number of FS sheets via hole doping decreases the EPC channels, resulting in a decrease of T_c . Interestingly, the hole doping in fcc LaH₁₀ slightly increases T_c from 233 K (without hole doping) to 245 K at $n_h = 0.3e$ (see Table SI). We note that for $n_h = 0.3e$, the predicted T_c value of fcc LaH₁₀ is still lower than that of fcc YH₁₀ by 24 K. Considering that both the hole-doped systems with $n_h = 0.3e$ have the same number of FS sheets, it is implied that fcc YH₁₀ would have larger electron-phonon matrix elements than fcc LaH₁₀.

In conclusion, our first-principles calculations for fcc LaH₁₀ have shown that the hybridized states of La and H₁ atoms as well as H₁ and H₂ atoms on the four FS sheets are strongly coupled with the phonon modes in the whole frequency range, contrasting with a typical low- T_c BCS-type superconductor MgB₂ [43] where certain phonon modes significantly contribute to the EPC. Specifically, we revealed that the presence of such multiple FS sheets with different orbital characters gives rise to the two nodeless, anisotropic superconducting gaps on the FS. It is thus demonstrated that the two factors such as multiband pairing and the hybridized states of constituent atoms play crucial roles in determining the recently observed [1, 2] room-temperature SC in fcc LaH₁₀.

The present findings have important implications for understanding the underlying mechanisms involved in high- T_c SC of compressed hydrides, as well as in tuning T_c through carrier doping.

Acknowledgement. This work was supported by the National Research Foundation of Korea (NRF) grant funded by the Korean Government (Grants No. 2019R1A2C1002975, No. 2016K1A4A3914691, and No. 2015M3D1A1070609). The calculations were performed by the KISTI Supercomputing Center through the Strategic Support Program (Program No. KSC-2018-CRE-0063) for the supercomputing application research.

* Corresponding author: chojh@hanyang.ac.kr

-
- [1] M. Somayazulu, M. Ahart, A. K. Mishra, Z. M. Geballe, M. Baldini, Y. Meng, V. V. Struzhkin, and R. J. Hemley, *Phys. Rev. Lett.* **122**, 027001 (2019).
 - [2] A. P. Drozdov, P. P. Kong, V. S. Minkov, S. P. Besedin, M. A. Kuzovnikov, S. Mozaffari, L. Balicas, F. F. Balakirev, D. E. Graf, V. B. Prakapenka, E. Greenberg, D. A. Knyazev, M. Tkacz, and M. I. Eremets, *Nature (London)* **569**, 528 (2019).
 - [3] A. P. Drozdov, M. I. Eremets, I. A. Troyan, V. Ksenofontov, and S. I. Shylin, *Nature (London)* **525**, 73 (2015).
 - [4] C. M. Pépin, G. Geneste, A. Dewaele, M. Mezouar, and P. Loubeyre, *Science* **357**, 382 (2017).
 - [5] X. Li, X. Huang, D. Duan, C. J. Pickard, D. Zhou, H. Xie, Q. Zhuang, Y. Huang, Q. Zhou, B. Liu, and T. Cui, *Nat. Comm.* **10**, 3461 (2019).
 - [6] I. A. Troyan, D. V. Semenov, A. G. Kvashnin, A. G. Ivanova, V. B. Prakapenka, E. Greenberg, A. G. Gavriliuk, I. S. Lyubutin, V. V. Struzhkin, and A. R. Oganov, arXiv:1908.01534.
 - [7] E. Zurek and T. Bi, *J. Chem. Phys.* **150**, 050901 (2019).
 - [8] J. A. Flores-Livas, L. Boeri, A. Sanna, G. Profeta, R. Arita, and M. Eremets, arXiv:1905.06693.
 - [9] J. Bardeen, L. N. Cooper, and J. R. Schrieffer, *Phys. Rev.* **106**, 162 (1957).
 - [10] N. W. Ashcroft, *Phys. Rev. Lett.* **21**, 1748 (1968).
 - [11] J. McMinis, R. C. Clay, D. Lee, and M. A. Morales, *Phys. Rev. Lett.* **114**, 105305 (2015).
 - [12] J. M. McMahon, M. A. Morales, C. Pierleoni, and D. M. Ceperey, *Rev. Mod. Phys.* **84**, 1607 (2012).
 - [13] R. P. Dias and I. F. Silvera, *Science* **355**, 715 (2017).
 - [14] W. A. Bassett, *High Press. Res.* **29**, 163 (2009).
 - [15] H. K. Mao, X. J. Chen, Y. Ding, B. Li, and L. Wang, *Rev. Mod. Phys.* **90**, 015007 (2018).
 - [16] H. Wang, J. S. Tse, K. Tanaka, T. Litaka, and Y. Ma, *Proc. Natl. Acad. Sci. USA* **109**, 6463 (2012).
 - [17] D. Duan, Y. Liu, F. Tian, D. Li, X. Huang, Z. Zhao, H. Yu, B. Liu, W. Tian, and T. Cui, *Sci. Rep.* **4**, 6968 (2014).
 - [18] X. Feng, J. Zhang, G. Gao, H. Liu, and H. Wang, *RSC Adv.* **5**, 59292 (2015).
 - [19] Y. Quan and W. E. Pickett, *Phys. Rev. B* **93**, 104526 (2016).
 - [20] C. Heil, S. Cataldo, G. B. Bachelet, and L. Boeri, *Phys. Rev. B* **99**, 220502(R) (2019).
 - [21] F. Peng, Y. Sun, C. J. Pickard, R. J. Needs, Q. Wu, and Y. Ma, *Phys. Rev. Lett.* **119**, 107001 (2017).
 - [22] H. Liu, I. I. Naumov, R. Hoffmann, N. W. Ashcroft, and R. J.

- Hemley, Proc. Natl. Acad. Sci. USA **114**, 6990 (2017).
- [23] L. Liu, C. Wang, S. Yi, K. W. Kim, J. Kim, and J.-H. Cho, Phys. Rev. B **99**, 140501(R) (2019).
- [24] I. A. Kruglov, D. V. Semenov, R. Szczeniński, M. M. D. Esfahani, A. G. Kvashnin, and A. R. Oganov, arXiv:1810.01113.
- [25] Y. Quan, S. S. Ghosh, W. E. Pickett, arXiv:1906.02695.
- [26] C. Wang, S. Yi, and J.-H. Cho, Phys. Rev. B **100**, 060502(R) (2019).
- [27] P. Hohenberg and W. Kohn, Phys. Rev. **136**, B864 (1964); W. Kohn and L. J. Sham, Phys. Rev. **140**, A1133 (1965).
- [28] A. B. Migdal, Sov. Phys. JETP **34**, 996 (1958).
- [29] G. M. Eliashberg, Sov. Phys. JETP **11**, 696 (1960).
- [30] P. B. Allen and B. Mitrović, Solid State Phys. **37**, 1 (1982).
- [31] Our DFT calculations were performed using the Vienna *ab initio* simulation package (VASP) with the projector-augmented wave (PAW) method [32–34]. For the exchange-correlation energy, we employed the generalized-gradient approximation functional of Perdew-Burke-Ernzerhof (PBE) [35]. A plane-wave basis was taken with a kinetic energy cutoff of 500 eV, and the \mathbf{k} -space integration was done with $24 \times 24 \times 24$ k points for the structure optimization. All atoms were allowed to relax along the calculated forces until all the residual force components were less than 0.001 eV/Å. The lattice dynamics and EPC calculations were carried out by using the QUANTUM ESPRESSO (QE) package [36] with the optimized norm-conserved Vanderbilt pseudopotentials (ONCV) [37] (see Fig. S7 in the Supplemental Material [41]) and a plane-wave cutoff of 1224 eV. Here, we used the $6 \times 6 \times 6$ q points and $24 \times 24 \times 24$ k points for the computation of phonon frequencies. For the calculation of EPC, we used the software EPW [38–40] with the $24 \times 24 \times 24$ q points and $72 \times 72 \times 72$ k points.
- [32] G. Kresse and J. Hafner, Phys. Rev. B **48**, 13115 (1993).
- [33] G. Kresse and J. Furthmüller, Comput. Mater. Sci. **6**, 15 (1996).
- [34] P. E. Blöchl, Phys. Rev. B **50**, 17953 (1994).
- [35] J. P. Perdew, K. Burke, and M. Ernzerhof, Phys. Rev. Lett. **77**, 3865 (1996); **78**, 1396 (1997).
- [36] P. Giannozzi, S. Baroni, N. Bonini, M. Calandra, R. Car, C. Cavazzoni, D. Ceresoli, G. L. Chiarotti, M. Cococcioni, I. Dabo *et al.*, J. Phys.: Condens. Matter **21**, 395502 (2009).
- [37] M. J. van Setten, M. Giantomassi, E. Bousquet, M. J. Verstraete, D. R. Hamann, X. Gonze, and G. M. Rignanese, Comput. Phys. Commun. **226**, 39 (2018).
- [38] F. Giustino, M. L. Cohen, and S. G. Louie, Phys. Rev. B **76**, 165108(R) (2007).
- [39] E. R. Margine and F. Giustino, Phys. Rev. B **87**, 024505 (2013).
- [40] S. Poncé, E. R. Margine, C. Verdi, and F. Giustino, Comput. Phys. Commun. **209**, 116 (2016).
- [41] See Supplemental Material at <http://link.aps.org/supplemental/xxxxx> for the band projections onto the orbitals of La, H₁, and H₂ atoms in fcc LaH₁₀ and fcc YH₁₀. The estimation of T_c using the anisotropic Migdal-Eliashberg equations, the band structure of fcc YH₁₀ with hole doping, and the band structures of fcc LaH₁₀ and fcc YH₁₀ obtained using PAW+PBE pseudopotentials in VASP and ONCV+PBE pseudopotentials in QE are also given.
- [42] P. B. Allen and R. C. Dynes, Phys. Rev. B **12**, 905 (1975).
- [43] Y. Kong, O. V. Dolgov, O. Jepsen, and O. K. Andersen, Phys. Rev. B **64**, 020501(R) (2001).

Supplemental Material for Multiband Nature of the Room-Temperature Superconductivity in Compressed LaH₁₀

1. Band projections onto the orbitals of La, H₁, and H₂ atoms in fcc LaH₁₀.

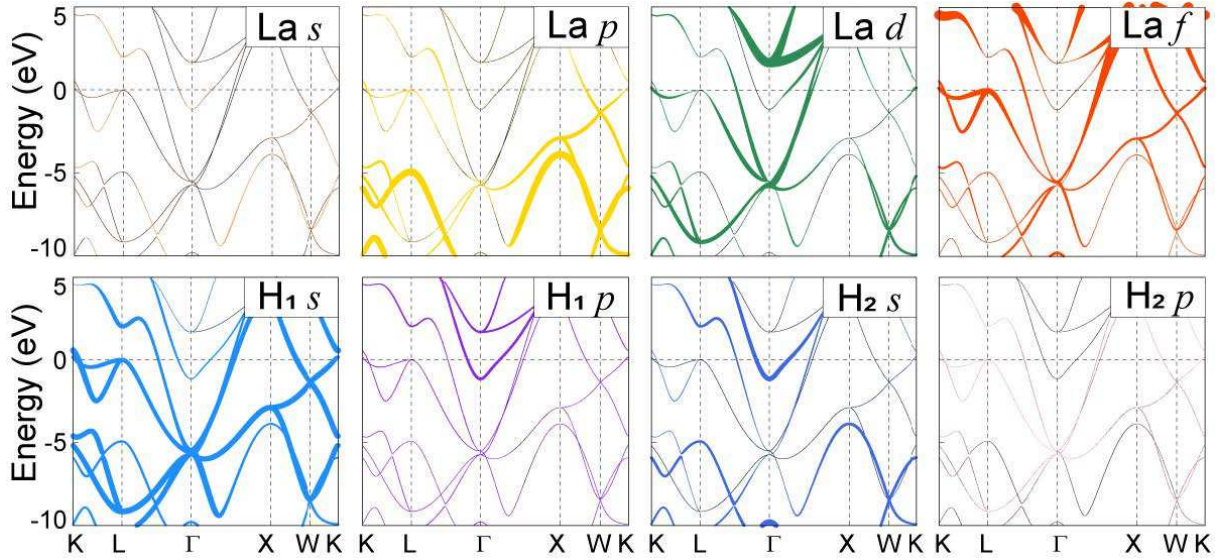


FIG. S1: Calculated bands projected onto the La s , La p , La d , La f , H₁ s , H₁ p , H₂ s , and H₂ p orbitals in fcc LaH₁₀. Here, the radii of circles are proportional to the weights of the corresponding orbitals.

2. Estimation of T_c using the anisotropic Migdal-Eliashberg equations.

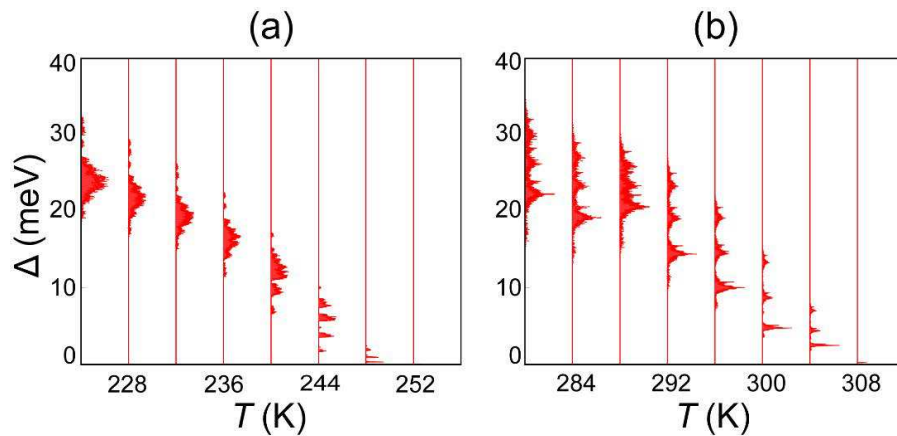


FIG. S2: Calculated anisotropic superconducting gap Δ of (a) fcc LaH₁₀ and (b) fcc YH₁₀ near T_c .

3. Optimized structure of the fcc phase of compressed YH₁₀.

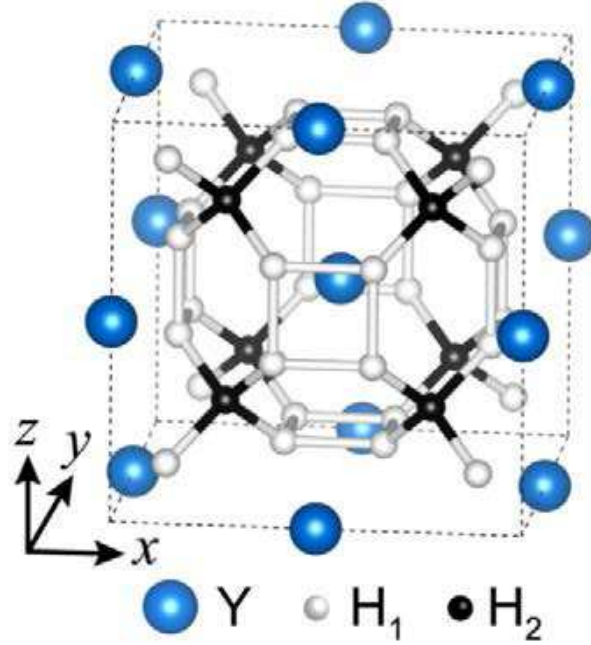


FIG. S3: Optimized structure of the fcc phase of compressed YH₁₀, composed of the cages of 32 H atoms surrounding a Y atom. The two different types of H atoms, i.e., H₁ and H₂, are drawn with bright and dark circles, respectively. The positive x , y , and z axes point along the [001], [010], and [001] directions, respectively. The lattice parameters are $a = b = c = 4.598$ Å at 300 GPa.

4. Band projections onto the orbitals of Y, H₁, and H₂ atoms in fcc YH₁₀.

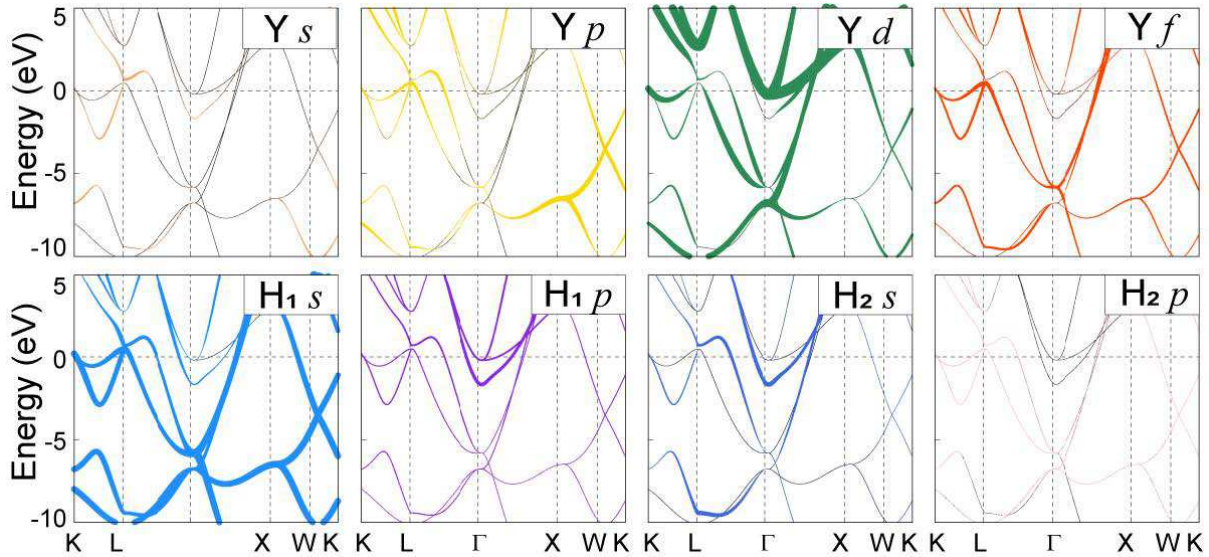


FIG. S4: Calculated bands projected onto the Y s , Y p , Y d , Y f , H₁ s , H₁ p , H₂ s , and H₂ p orbitals in fcc YH₁₀. Here, the radii of circles are proportional to the weights of the corresponding orbitals.

5. Projection of $\lambda_{n\mathbf{k}}$ on each FS sheet of fcc YH₁₀.

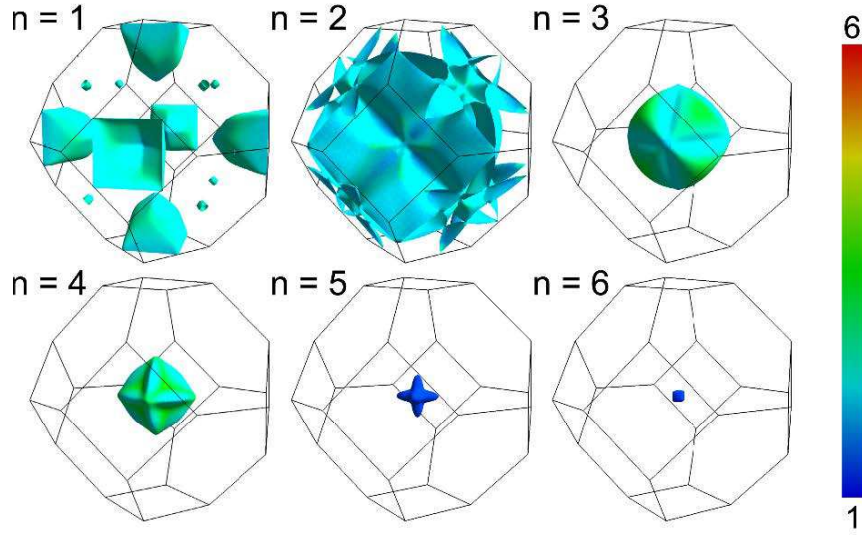


FIG. S5: Projection of $\lambda_{n\mathbf{k}}$ on the six Fermi surface sheets of fcc YH₁₀.

6. Band structure of fcc YH₁₀ with hole doping.

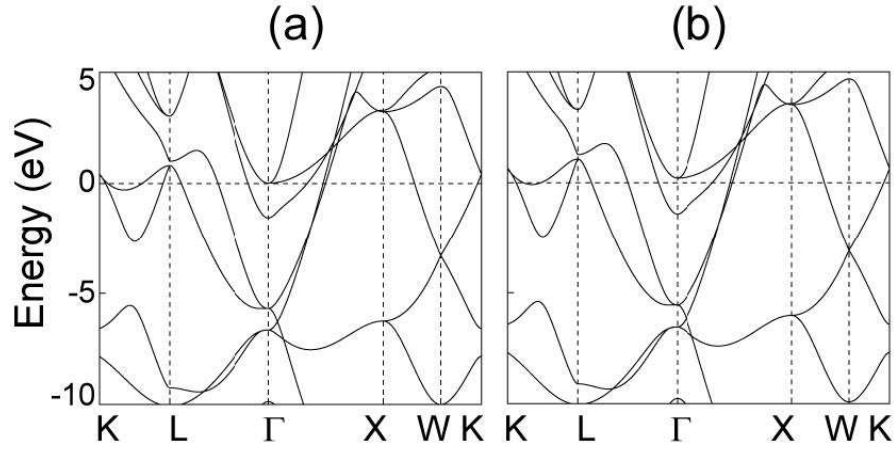


FIG. S6: Calculated band structures of fcc YH₁₀ with the amount of hole doping $n_h =$ (a) $0.17e$ and (b) $0.3e$ per unit cell.

7. Band structures of fcc LaH_{10} and fcc YH_{10} , obtained using PAW+PBE pseudopotentials in VASP and ONCV+PBE pseudopotentials in QE.

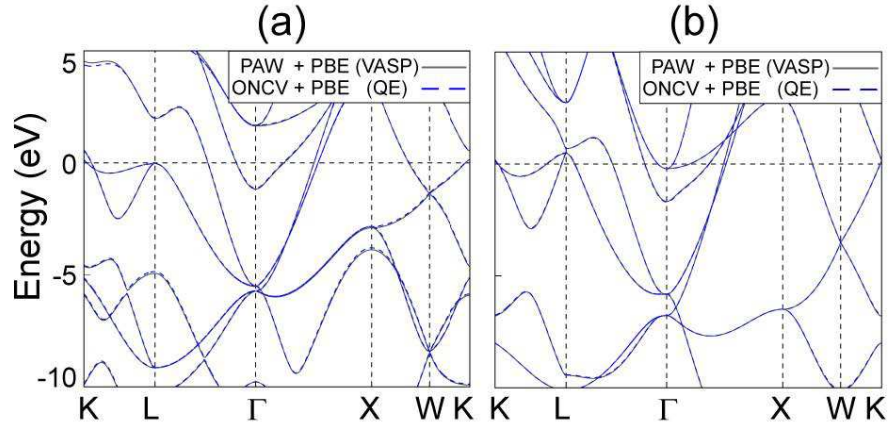


FIG. S7: Calculated electronic band structures of (a) fcc LaH_{10} and (b) fcc YH_{10} at 300 GPa. The two results obtained using PAW+PBE pseudopotentials in VASP (grey lines) and ONCV+PBE pseudopotentials in QE (blue dashed lines) overlap for comparison. We note that (i) the lattice constants optimized using PAW+PBE pseudopotentials in VASP and ONCV+PBE pseudopotentials in QE change only by less than 0.1%, and (ii) the band structures obtained using the two different pseudopotentials are nearly the same with each other, especially near the Fermi energy.

Table SI. Calculated λ and T_c values of fcc YH_{10} as a function of hole doping.

TABLE I: Calculated λ and T_c values of fcc YH_{10} at $n_h = 0.1, 0.2,$ and $0.3e$ per unit cell using the isotropic Migdal-Eliashberg formalism with $\mu^* = 0.13$. For comparison, the corresponding values of fcc LaH_{10} are given in parentheses. The results without hole doping are also given in the line of $n_h = 0$.

n_h ($e/\text{unit cell}$)	λ	T_c (K)
0	2.23 (1.86)	290 (233)
0.1	2.11 (1.89)	282 (235)
0.2	2.00 (1.97)	275 (239)
0.3	1.91 (2.11)	269 (245)